Thermodynamic, electronic, and optical properties of graphene oxide: A statistical *ab initio* approach

I. Guilhon,[1,2] F. Bechstedt,[1] Silvana Botti,[1] M. Marques,[2] and L. K. Teles[2]

[1]*Institut für Festkörpertheorie und -optik, Friedrich-Schiller-Universität Jena and ETSF, Max-Wien-Platz 1, D-07743 Jena, Germany*

[2]*Grupo de Materiais Semicondutores e Nanotecnologia, Instituto Tecnológico de Aeronáutica, DCTA, 12228-900 São José dos Campos, Brazil*

(Received 5 April 2017; published 23 June 2017)

We study the incomplete oxidation of graphene or reduction of graphene oxide for hydroxyl and epoxy oxidant groups. While in wet oxidation hydroxyl groups are favorable, in a drier environment an oxygen atom can bridge two neighboring carbon atoms. We model composition variations and structural disorder within a statistical theory, the generalized quasichemical approximation, combined with density functional theory calculations of the local atomic geometries. A generalization of the statistical approach is developed to account for the antiparallel orientation of hydroxyl groups and a fourfold coordination of C atoms. The theoretical framework enables a thermodynamic treatment of graphene oxide as a function of oxygen content, allowing us to derive temperature-composition phase diagrams and investigate possible clustering and segregation. The resulting geometries, local and average electronic structures, and optical absorption spectra are discussed and compared with available experimental data.

DOI: 10.1103/PhysRevB.95.245427

I. INTRODUCTION

Graphene's unique electronic and mechanical properties are tightly related to its two-dimensional (2D) structure and the nature of C-C bonds. The graphene functionalization to obtain modified properties has attracted a large interest since the first discovery of graphene [1,2]. One material of this 2D family is graphene oxide (GO) [3–6], which is of interest mainly in two research directions. Chemical reduction of GO is one important way for the high-yield production of graphene [7]. At the same time, GO has been demonstrated to be a material with a great application potential in different fields, such as 2D electronics [8–10] and optoelectronics [4,11], sensor devices [12,13], and energy storage as supercapacitor electrodes [14]. In particular, the band-gap opening [15] makes GO also a promising 2D material as a chemically tunable platform for optical and optoelectronic applications in the visible-light region [4,16]. This, however, requires detailed investigations of its optical properties.

GO can be exfoliated from graphite oxide, which was synthesized about 150 years ago, as Brodie investigated the reactivity of graphite flakes [17]. Indeed, the production of graphene by chemical reduction of exfoliated GO sheets has been explored extensively [5]. GO is typically synthesized from graphite powder using chemical solutions with strong oxidant compounds [5]. However, the opposite approach is also possible. The chemical functionalization of graphene within wet chemistry also leads to oxidized samples [3]. In addition, nonchemical methods are applicable. Indeed, graphene exposed to oxygen plasma has been reported as a successful way to obtain GO samples [15].

Despite the strong research effort that has been devoted to explore the stoichiometry and atomic structure of GO, theoretically and experimentally, the details of the GO structure are still under debate [3,5,18]. There is only agreement that graphene oxide can be considered as an insulating, but disordered, analog of the highly conducting crystalline graphene [4].

Magnetic resonance experiments have indicated that the atomic layer of carbon atoms is mainly oxidized with hydroxyl (-OH) and epoxy (-O-) groups on the basal plane [19]. At edge sites even carboxylic acid groups (-COOH) may occur [20]. The basic structural models for decoration of the basal plane of carbon atoms by hydroxyls and peroxides have already been derived for graphite oxide by Hofmann and Holst [21] or Ruess [22]. However, also models containing mixtures of both oxidant groups have been suggested [20,23]. For a review, the reader is referred to Ref. [6].

The arrangement of different oxygen-containing groups above and below a carbon basal plane, and their mixture, gives origin to some structural disorder [4]. Besides the structural disorder, graphene oxide layers also undergo a variation of the oxygen stoichiometry [4], i.e., are chemically disordered. When reduction methods are applied to GO sheets in order to produce graphene samples [24], different C/O ratios can be obtained according to the reduction method used [7]. Among the different alternatives to promote the reduction of a GO sample, one can distinguish the thermal reduction and chemical reduction [7]. The different degree of remaining oxidation and the distribution of oxide groups give rise to samples with very distinct electronic properties. These observations make graphene oxide a natural candidate for band gap engineering over a broad range of wavelengths, owing to its composition-dependent electronic structure [4,15,25,26]. The reduction of GO sheets or the incomplete oxidation of graphene layers can deliver 2D materials with properties that can be tuned for specific applications by controlling chemical composition and geometry.

The ability to prepare GO samples with varying chemical composition and arrangement of hydroxyl and epoxy groups with control over their properties is still a big challenge [27]. In order to achieve such samples, a deeper understanding is needed of thermodynamic aspects, oxidation/reduction processes, stoichiometry, and the geometrical relationship to the electronic properties that one would like to control. Theoretical studies from first principles of the thermodynamic stability and the dependence of electronic structure and optical

properties are helpful in this respect. Indeed, this has been shown for the epoxide reduction [28], the structure of graphene oxide [29], the electronic properties [25,26], and the band gap engineering [15,16]. However, many open questions remain concerning the influence of structural and chemical disorder on energetics, electronic structure, and optical absorption.

In this paper, we present a rigorous first-principles study of GO as a function of its intermediate oxidation level, considering both hydroxyl and epoxy as oxidant groups. A clear picture of the relationship between the thermodynamic stability of homogenous phases and its consequences for the estimated physical properties is presented. The statistical approach that we use, called the generalized quasichemical approximation, is based on cluster expansion. It has been successfully applied to 2D and 3D alloyed systems [30–35]. The estimation of the system entropy by such an approach is revisited and generalized in a formalism that dismisses combinatoric arguments. The electronic and optical properties of the stable geometries are computed as functions of the oxidation level including structural and chemical disorder. The obtained results cover the whole range of possible oxidation levels by the considered oxidant groups. They are compared with experimental findings whenever it is possible.

II. METHODOLOGY

A. Statistical approach to functionalized 2D sheets

The chemical and structural disorder due to the distribution of oxidant groups adsorbed on a graphene (C) layer or a not fully oxidized graphene sheet is modeled within the generalized quasichemical approximation (GQCA). The alloy system is expanded in clusters with n atomic sites, which are by hypothesis statistically and energetically independent [36]. Each arrangement is associated with a set of physical properties obtained from a repetition of the considered cluster along the whole atomic layer. This approximation is more realistic as the clusters become larger. However, the number of the possible configurations to be studied increases exponentially with the number of sites in the supercell. Therefore, the cluster size must be chosen considering a compromise between precision and the number of configurations to be taken into account.

In the case of substitutional $A_{1-x}B_x$ alloys of average composition x only atoms of type A are replaced by atoms of type B in the entire atomic lattice or only in a sublattice. The total number of atoms is however conserved. Here, in the case of oxidation by hydroxyl, -OH groups are adsorbed by carbon atoms, whereas, if the oxidant is epoxy, -O- bridges a pair of carbon atoms. Sites, or pairs of sites, in the graphene lattice are therefore modified. Considering constraints concerning the orientation of adjacent -OH groups or the maximal fourfold coordination of carbon atoms, the GQCA has to be generalized as described below.

Even though the GQCA is commonly used to describe substitutional alloys, its adaptation to other disordered systems, such as functionalized sheets, is straightforward. In order to make the treatment and the results clearer, we consider each oxidant group separately.

The resulting different possible atomic arrangements can be organized into J nonequivalent cluster classes, by considering all the space group symmetry operations. Different degeneracy numbers g_j are attributed to each cluster class to account for the number of atomic arrangements that generate periodic 2D systems equivalent by symmetry. The statistical treatment of the atomic arrangements is performed according to the temperature (T) and composition (x) dependent probability $x_j = x_j(x,T)$ for the realization of each class $j = 1,2,\ldots,J$, allowing us to define average properties and thermodynamic quantities.

The equilibrium state of a disordered system can be determined by the minimization of the Gibbs free energy G, which can be approximated by the Helmholtz free energy F for solid systems under pressures around 1 atmosphere [36]. This is a good approximation for substitutional alloys with a fixed number of atoms. In general, here we have the same number of carbon atoms in all clusters but a varying number $n_{O,j}$ of oxidant (hydroxyl or epoxy) groups. Partially oxidized graphene or reduced graphene oxide can be modeled considering composition-weighted graphene and graphene oxide, i.e., assuming completely oxidized graphene as reservoir for the oxidant groups. Then, the studied system can be considered as a combination between pristine graphene and fully oxidized graphene, within an analogous formalism to that for a binary alloy. From above, we conveniently define the mixing free energy ΔF as the deviation from the Helmholtz free energy of the system with a partial oxidation level x from the weighted average between graphene and the fully oxidized sheets as

$$\Delta F(x,T) = F(x,T) - xF_{GO}(T) - (1-x)F_C(T), \qquad (1)$$

where the oxidation level x is defined as the fraction of carbon atoms in the sheet bonded to oxidant groups, and F_{GO} and F_C are the free energies of graphene oxide and graphene, respectively.

The mixing Helmholtz free energy can be decomposed into an internal energy term (ΔU) and an entropy contribution (ΔS) as $\Delta F = \Delta U - T\Delta S$. The internal mixing energy ΔU can be estimated as

$$\Delta U = \sum_{j=1}^{J} M_j E_j - M[xE_{GO} + (1-x)E_C], \qquad (2)$$

where M_j is the number of clusters, which belong to the equivalent class j in the system with $x_j = M_j/M$, $M = \sum_{j=1}^{J} M_j$ is the total number of clusters in the system, and E_j is the total energy of a cluster that belongs to cluster class j. E_C and E_{GO} are respectively the internal energy per cluster calculated from cluster configurations that correspond to graphene and the most stable fully oxidized cluster class(es).

The energetics of cluster configurations with intermediate oxidation levels can be further investigated considering excess energies ΔE_j with respect to the number of oxygen groups per cluster $n_{O,j}$. This quantity is defined as

$$\Delta E_j = E_j - \left(\frac{n_{O,j}}{n}E_{GO} + \frac{n - n_{O,j}}{n}E_C\right), \qquad (3)$$

where $n_{O,j}$ is the number of oxygen groups in the cluster class j and n is the number of oxygen groups per cluster in the (fully oxidized) graphene oxide system with $x = 1$.

In previous works, the entropy of an alloyed system has been derived from the number of possible combinations between different elements [30,32,33]. Hence, the correction of the system entropy referring to the cluster distribution is obtained from combinatorics arguments [37]. However the calculation of the exact number of configurations of epoxides, which are a multisite (pair) adsorption groups, on a graphene sheet is not a trivial problem, and different approximate solutions have been proposed to this problem [38,39]. Indeed, the difficulty in the analysis of a multisite statistics has been addressed for dimer adsorption on various 2D lattices [38]. The introduction of structural constraints on the adsorption of hydroxyl groups also results in a nontrivial number of allowed arrangements.

Recently, we suggested a formulation of the mixing entropy only on the base of the cluster probabilities x_j and the class degeneracies g_j [34]. It combines the expression of the configurational entropy within the ideal-solid solution approach [36] with the entropy correction of the GQCA for alloys written as the Kullback-Leibler divergence [40] between the ideal random probability distribution of the clusters x_j^o from the x_j distribution which minimizes the mixing free energy $\Delta F(x,T)$ [34].

To avoid the problem of considering nontrivial combinatorics, we have derived an entropy expression based on the Shannon entropy per cluster for a given probability distribution x_j and a set of cluster class degeneracies g_j. Supposing that all the different instances of a symmetry class j are equiprobable, we assign a probability $p_{l,j} = x_j/g_j$ to each possible atomic arrangement l that belongs to cluster class j. The Shannon entropy [41] per cluster is then calculated as

$$\frac{\Delta S}{M} = -k_b \sum_{k,l} p_{l,j} \ln(p_{l,j}), \tag{4}$$

where k_b is the Boltzmann constant. This expression can be rewritten as the total configurational entropy as

$$\Delta S = k_b M \sum_{j=1}^{J} x_j (\ln g_j - \ln x_j). \tag{5}$$

This formula is simpler than the previously considered entropy expressions [30,32,37], but reproduces the same results in the thermodynamic limit with no need of combinatorics arguments (see the Appendix).

Finally, the excess free energy expression per cluster that must be minimized by the probability distribution x_j among the cluster classes is given by the expression

$$\frac{\Delta F}{M} = \sum_{j=1}^{J} x_j E_j - [x E_{GO} + (1-x) E_C] - k_b T \sum_{j=1}^{J} x_j (\ln g_j - \ln x_j). \tag{6}$$

The set of probabilities x_j must fulfill two constraints, (i) the normalization of the sum of all probabilities, $\sum_{j=1}^{J} x_j = 1$, and (ii) the average number of oxygen groups per cluster $\overline{n_O} = nx$ in the system, $\sum_{j=1}^{J} x_j n_{O,j} = \overline{n_O}$. The constrained minimization of the excess free energy per cluster $\Delta F/M$, given by Eq. (6), with respect to the probability distribution over the clusters can be obtained by using the Lagrange multiplier formalism, leading to the following distribution of occurrence probability

$$x_j = \frac{g_j \lambda^{n_{O,j}} \exp\left(-\frac{E_j}{k_b T}\right)}{\sum_{j=1}^{J} g_j \lambda^{n_{O,j}} \exp\left(-\frac{E_j}{k_b T}\right)}, \tag{7}$$

where λ is a numerical constant related to the Lagrange multiplier associated with the average oxidation level. Its value can be calculated by solving the polynomial equation

$$\sum_{j=1}^{J} g_j (n_{O,j} - \overline{n_O}) \lambda^{n_{O,j}} \exp\left(-\frac{E_j}{k_b T}\right) = 0. \tag{8}$$

Once the occurrence probability distribution is obtained, a property $P(x,T)$ of a certain alloy can be calculated as an average of the property values P_j of individual cluster classes j that are weighted by occurrence probabilities $x_j(x,T)$ as

$$P(x,T) = \sum_{j=1}^{J} x_j(x,T) P_j. \tag{9}$$

The thermodynamic stability is characterized by the construction of a T-x phase diagram from the minimized mixing free energy $\Delta F(x,T)$. The binodal and spinodal curves are constructed as described in Refs. [30,32]. Each point in the diagram represents one alloy with an oxidation level x at a temperature T. The binodal and the spinodal curves split the diagram into three regions, which correspond to stable, metastable, and unstable phases.

In the region below the spinodal curve the alloy decomposes into two homogeneous phases with distinct oxidation levels x_1 and x_2, and corresponding weights w_1 and w_2, thereby minimizing the mixing free energy $\Delta F(x,T)$ for given x and T [34]. Between the binodal and spinodal curves the alloys are metastable and the phase decomposition is hampered. The points above the binodal curve are considered to be stable homogeneous alloys. The critical temperature T_c is defined as the smallest temperature for which the system is still thermodynamically stable at any oxidation level.

B. *Ab initio* calculation methods

The total energies E_j and the physical properties P_j of interest of each cluster class j are calculated within the *ab initio* density functional theory (DFT) as implemented in the VASP code [42,43]. In order to use the periodic Born–von Karman boundary conditions, each cluster system is simulated as an artificial 3D array of atomic layers separated by distances of $L = 20$ Å, so that the interaction between different sheets vanishes. The in-plane unit cells are simulated by 2×2 graphene cells with 8 carbon atoms but with varying lateral lattice constant and an atomic basis, consisting of these atoms and the corresponding number of oxidant groups, as described below. The equilibrium atomic positions are relaxed until the Hellmann-Feynman forces are smaller than 0.01 eV Å^{-1}.

The exchange and correlation (XC) functional is described within the generalized gradient approximation (GGA), as proposed by Perdew-Burke-Ernzerhof (PBE) [44,45]. The pseudopotentials of the C, O, and H atoms are generated within the projector-augmented wave (PAW) method [46,47]. The wave functions between the cores are expanded in plane waves up to a kinetic energy cutoff of 450 eV. Integrals over the Brillouin zone (BZ) are computed considering a $9 \times 9 \times 1$ Γ-centered Monkhorst-Pack k-point mesh [48].

The pure DFT methodology for the ground state is well known for underestimating the energy gaps and, in general, all other interband transition energies, due to ignoring the nonlocality of the exact XC functional and energy-dependent quasiparticle self-energy. In this sense, trustworthy predictions for electronic properties demand corrections of standard DFT calculations to take the excitation aspect into account [49,50]. Here, we simulate the quasiparticle corrections to obtain reasonable electronic structures by considering the HSE06 functional, a screened hybrid functional proposed by Heyd, Scuseria, and Ernzerhof for solids [51,52]. The exchange-correlation potential derived from this hybrid functional accounts for an important property of the XC self-energy, its spatial nonlocality, which corrects the interband transition energies [50].

We calculate the energy band gap for the 2D periodic systems associated with each cluster class neglecting spin-polarization effects. The semiconductor and insulator fundamental energy gaps are considered for the GQCA averages, while metallic behavior is identified as the zero-energy gap. Configurations with an odd number of electrons are discussed in detail considering spin-polarized PBE calculations to check the results obtained from non-spin-polarized calculations.

The optical properties are described by the frequency-dependent dielectric matrix, which is calculated within the independent-quasiparticle approximation [53]. The optical transition matrix elements are described adopting the longitudinal gauge [54] as

$$M_{cv}(\vec{k},\hat{q}) = \lim_{\vec{q}\to\vec{0}} \frac{1}{|\vec{q}|} \langle c\vec{k}| \, e^{i\vec{q}\cdot\vec{r}} \, |v\vec{k}+\vec{q}\rangle \, . \tag{10}$$

In general, the optical spectra are also influenced by excitonic effects [50]. However, in 2D systems there is a partial compensation of quasiparticle blueshifts and exciton redshifts. This has been clearly demonstrated for graphene [55] and 2D systems with large energy gaps such as hBN [56].

Therefore, the dielectric function for vanishing photon momentum $\hat{q}$ and photon energy $\hbar\omega$ is calculated by

$$\epsilon(\hat{q},\omega) = 1 + \frac{4\pi e^2}{V} \sum_{c,v} \sum_{\vec{k}} \frac{|M_{cv}(\vec{k},\hat{q})|^2}{\varepsilon_c(\vec{k}) - \varepsilon_v(\vec{k}) - \hbar\omega - i\eta}, \tag{11}$$

where $\varepsilon_v(\vec{k})$ [$\varepsilon_c(\vec{k})$] is the eigenvalue associated with an occupied (unoccupied) state in a valence (conduction) band associated with the Bloch wave vector $\vec{k}$, and η is a broadening parameter. Because of the representation $\epsilon(\hat{q},\omega) = \sum_{i,j=1}^{3} \hat{q}_i \epsilon_{ij}(\omega) \hat{q}_j$ the complete dielectric tensor can be derived, which allows the discussion of an arbitrary light polarization.

The calculated dielectric function of the artificial 3D periodic system is affected by the length L of the empty space between the atomic layers in the supercell approach. However, it can be traced back to the L-independent optical conductivity tensor by $\sigma_{ij}(\omega) = \frac{\omega}{4\pi i} L[\epsilon_{ij}(\omega) - \delta_{ij}]$. We study normal incidence of light and, hence, in-plane light polarization. The in-plane polarized light adsorption of the 2D layer can be characterized by the optical absorbance as

$$A(\omega) = \frac{\omega}{c} L \, \mathrm{Im}[\epsilon_{jj}(\omega)] \quad (j = x,y), \tag{12}$$

where c is the speed of light in vacuum. In general, this quantity is the real part of 2D optical conductivity. However, in the limit of vanishing reflectance it is identical to the absorbance [57].

Average absorbance spectra $A_{\mathrm{GQCA}}(\omega,x,T)$ are calculated from the occurrence probability distribution $x_j(x,T)$ among the clusters applying Eq. (9) for the absorbance of the different cluster classes for each photon energy. In cases where the system is decomposed into large oxygen-poor and -rich domains, a prediction of optical spectra $A_{PS}(\omega,x,T)$ considering a fully decomposition of the system in such phases can be done. The oxidation levels $x_1(T)$ and $x_2(T)$ of each phase are determined from the T-x phase diagram and the average absorbance spectrum is determined by a weighted average with the weights of the separated phases w_1 and w_2 [34].

III. RESULTS AND DISCUSSION

A. Graphene oxides

In order to describe completely oxidized graphene we study the two oxidant groups, epoxy and hydroxyl, separately. We start with the full hydroxyl decoration of graphene. Thereby, in the case of the adsorption of the -OH groups, we restrict their alternating bonding to the single carbon atoms on top and below the graphene sheet.

This leads to 8 -OH groups per 2×2 graphene unit cell as illustrated in Fig. 1(a) (generalized Ruess model [5]). In the case of graphene oxide decorated only by epoxy groups, we investigate the possible arrangement of these groups on both sides of the graphene sheet. Thereby, one oxygen atom bridges two carbon atoms along one carbon sp^2 bond (generalized Hofmann model [5]). Consequently, no adjacent C-C bonds can be occupied by another oxygen atom. The constraints of alternate bonding (hydroxyls) and fourfold-coordinated carbon atoms (epoxides) are kept for a reasonable number of significant atomic arrangements with oxidant groups.

In the case of hydroxyl groups a 2×2 unit cluster contains 8 -OH groups which occupy the $n_S = n_{\mathrm{OH}} = 8$ carbon sites in an alternating manner as illustrated in Fig. 1(a). The configuration is used as an example of labeling and is further explained in the caption, following the defined labels and symbols. We avoid atomic configurations with too large formation energies. These thermodynamically unfavorable arrangements with small statistical weights in the GQCA approach are atomic arrangements with two neighboring hydroxyl groups bonded to the same side of the carbon sheet. This disregard was verified by comparing the total energies of the clusters $000000++$ and $000000+-$ with two hydroxyl groups at adjacent carbon sites in parallel or antiparallel orientation.

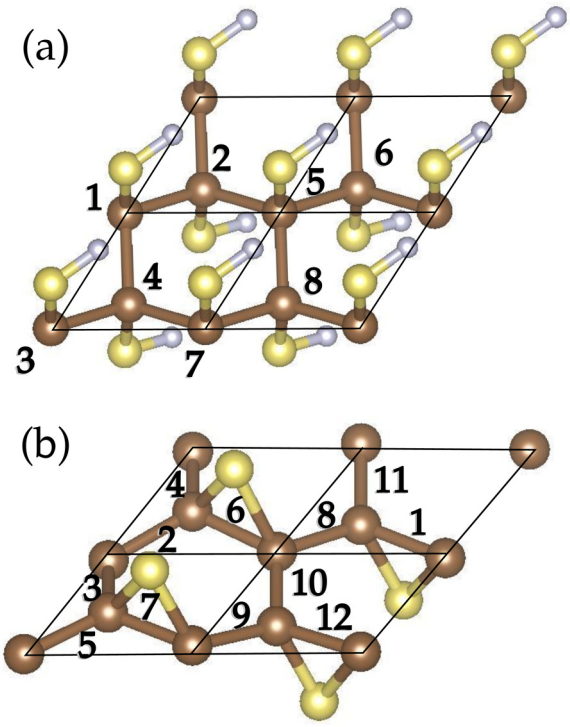

FIG. 1. Illustration of cluster configurations of graphene with a maximum number of oxidant groups: (a) $n_{OH} = 8$ alternately bonded hydroxyl groups and (b) $n_{epo} = 4$ epoxy groups. Carbon, oxygen, and hydrogen atoms are respectively represented by brown, golden, and gray spheres. The atomic sites and carbon-carbon bonds are labeled with integer numbers from 1 to 8 and from 1 to 12, respectively, according to the illustrations. Carbon sites or bonds without oxygen groups are represented as 0, oxygen groups above the graphene layer as +, and oxygen groups below the graphene layer as −. Consequently, the represented atomic arrangements are (a) $+-+-+-+-$, and (b) $-0000+ +0000-$.

The repulsive interaction between two neighboring hydroxyl groups at the same side of the sheet results in an energy increase of 1.31 eV/cluster. The strong electrostatic repulsion between neighboring hydroxyl groups is due the large electronegativity of oxygen compared with the hydrogen and carbon values [58]. The negatively charged oxygen ions in the -OH group are responsible for the repulsion if they come too close to each other.

Because of the pairing character of the oxidation by epoxy groups, we have to count $n_B = 12$ carbon-carbon bonds per cluster because of the constraint for threefold or fourfold coordination of carbon atoms. Only four bridging -O- groups can be adsorbed by 2×2 clusters in total. Each carbon is only allowed to bond to one epoxide group. Since neighboring C-C bonds cannot be occupied by -O-, the repulsion of the negatively charged oxygen atoms is mitigated. Therefore, all the possible manners of arranging epoxide groups on both sheet sides are considered. One of these eight possible cluster atomic arrangements with epoxide groups $-0000+ +0000-$ is shown in Fig. 1(b) explaining also the labeling of the twelve C-C bonds.

In the GQCA formalism, presented in Sec. II A, the configurational entropy formula expressed in Eq. (5) allows us to impose different constraints and consider both substitutional alloys or group adsorption on sites or bonds in a unified theoretical formalism. Besides the chemical disorder due to fluctuating number of sites or bonds occupied by oxidant groups, also structural disorder, e.g., due to the arrangement of the oxidizing groups on both sides of the carbon layer, is taken into account.

In order to use the canonical ensemble the average number of oxygen groups per cluster in the system $\overline{n_O}$ can be characterized according to the oxidation level x, defined as the fraction of carbon atoms functionalized with oxygen atoms in the carbon sheet. For the hydroxyl (epoxy) oxidation process, the atom ratio C/O is given by $1/x$ $(2/x)$. In this sense x describes the average composition of the nonstoichiometric oxides $C_{1-x}(COH)_x$ or $C_{1-x}(CO_{1/2})_x$, depending on the oxidant group considered. A more general formalism that considers a grand-canonical ensemble with the number of oxygen groups determined by chemical environment conditions may be explored, but will be left as a future work.

Within the described framework the fully oxidized system with hydroxyl groups (in which $x = 1$) is a honeycomb structure with sp^3 hybridized carbons, labeled as $+-+-+-+-$ [cf. Fig. 1(a)]. This cluster configuration exhibits a lattice constant of $a_{COH} = 2.63$ Å, which is larger than graphene lattice constant $a_C = 2.47$ Å, leading to a lattice constant mismatch of 6.5%. Due to the tendency for sp^3 hybridization the carbon layer exhibits a buckling amplitude of $\Delta = 0.50$ Å . The obtained carbon-oxygen and oxygen-hydrogen bonds show respective lengths of $d_{CO} = 1.42$ Å and $d_{OH} = 0.99$ Å, which determine an angle of $\theta_{OH} = 107^\circ$ between them. The structural parameters are similar to those obtained using a 5×5 graphene supercell [29]. We investigated the influence of hydroxyl orientation on calculated energy gap for the fully decorated configuration, but no changes above 0.1 eV were observed.

The fully oxidized configuration in Fig. 2 exhibits a direct energy gap of 3.78 eV at the Γ point according to the HSE06 calculation, showing the potential of the oxygen groups to significantly change the electronic structure of the graphene sheet. The zero-gap semimetal graphene becomes as graphene oxide a wide-gap semiconductor or insulator as other functionalized graphene layers, e.g., hydrogenated graphene [59]. The obtained electronic band structure for this oxide is illustrated in Fig. 2(a). Other HSE calculations even suggest a larger gap of 4.32 eV [16].

Differently from the oxidation based on hydroxyl groups, a fully oxidized graphene sheet with epoxy groups is not unique. There are a total of 8 fully oxidized configurations with $n_{epo,j} = 4$ epoxide groups. The possible clusters exhibit different arrangements of epoxy groups with respect to which side of the carbon sheet the oxygen groups are bonded and in which ordering the epoxy groups are distributed along the carbon honeycomb structure. Because of such structural disorder, a statistical treatment is necessary even for a fully oxidized system, in which the occurrence probability of each configuration is determined by the cluster energetics and the cluster degeneracy. The equilibrium state is calculated by the minimization of the system free energy considering $x = 1$. The lattice constants of the fully oxidized configurations stand between 2.55 Å and 2.67 Å. They lead to a mean lattice

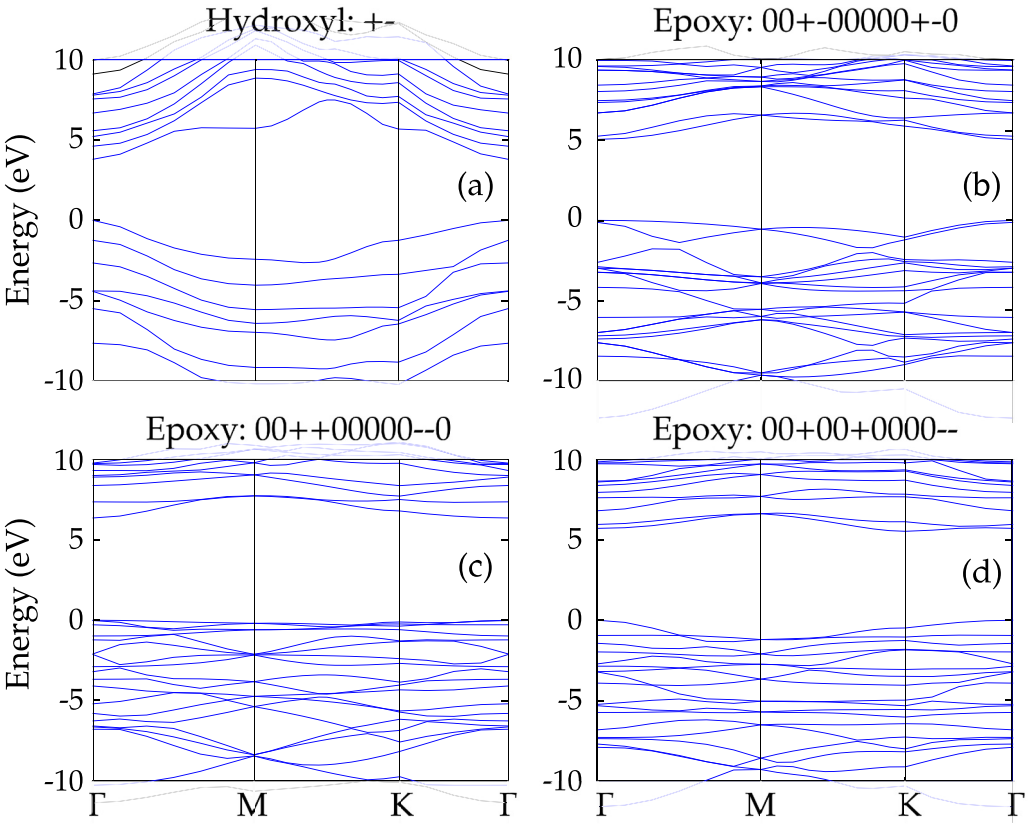

FIG. 2. Electronic band structures for fully oxidized cluster configurations ($x = 1$) obtained from HSE06 calculations: (a) carbon sheet completely oxidized with -OH groups is described within the 1×1 unit cell in order to avoid band folding associated with the use of the 2×2 supercell, and (b), (c), (d) thermodynamically favorable epoxy-oxidized systems studied within 2×2 supercells used in the cluster expansion of the disordered system. The valence band maximum (VBM) is chosen as energy reference.

constant of 2.57 Å at 200 °C. The average lattice mismatch in comparison to the pure graphene amounts to 4%. The graphene oxide layer possesses an average buckling amplitude of 0.36 Å at 200 °C and does not significantly change until temperatures of order 1100 °C. The epoxy groups are characterized by C-O bond lengths of 1.43 Å and a C-O-C bond angle close to 63° in rough agreement with calculations for isolated groups [28,29].

The band structures of the three most energetically stable configurations with $n_{\mathrm{epo},j} = 4$ are illustrated in Figs. 2(b)–2(d) for comparison. The different arrangements of the epoxy groups lead to distinct electronic structures. The fundamental energy gaps calculated for the $00+-00000+-0$, $00++00000--0$, and $00+00+0000--$ configurations are respectively 5.05, 6.37, and 5.50 eV from the HSE06 calculations. Both the direct Γ-Γ gap and the indirect Γ-K gap are observed in the studied configurations. Our gap findings are close to the HSE value of 6.2 eV found by Jiang *et al.* [16].

In Fig. 3, we show the in-plane components of the absorbance obtained from the DFT calculations for graphene and carbon sheets fully decorated with -OH or -O- groups as a function of the incident photon energy. While graphene and -OH decorated carbon sheet spectra are calculated directly from periodic structures, the illustrated spectra of the graphene fully oxidized with epoxy groups is obtained from a weighted average of the 8 possible epoxy arrangements in a 2×2 unit cell at $T = 300$ K. The absorbance spectrum of graphene exhibits an absorbance of $\pi\alpha$ (α is the Sommerfeld fine structure constant), while a very pronounced peak at about 4.0 eV is associated with the saddle point of the valence

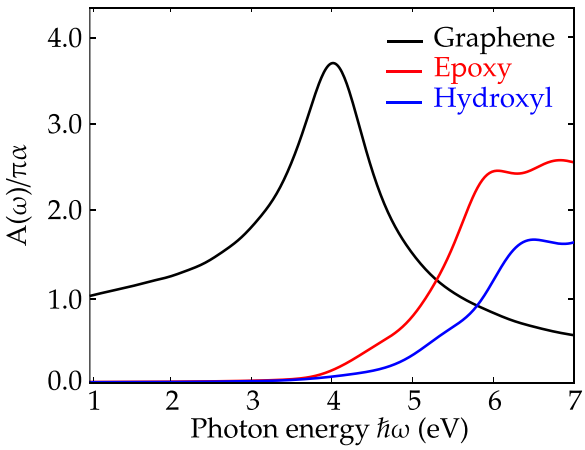

FIG. 3. Optical absorbance $A(\omega)$ of graphene (black curve), and carbon sheets fully decorated with hydroxyl (blue curve) or epoxy (red curve) groups as a function of the incident photon energy. The statistical weights of the different arrangements of configurations with $n_{\mathrm{epo},j} = 4$ are calculated considering a preparation temperature of $T = 300$ K.

and conduction π-band difference. These spectral features have been previously discussed in theoretical [32,60] and experimental [61] works. In the case of oxidized graphene sheets, the band gap opening forbids optical transitions for small photon energies and the sheets are transparent for low-energy radiation. For these materials, the optical absorbance significantly increases for photon energies above 4 eV in agreement with the calculated gaps.

B. Partial hydroxyl oxidation

The considered cluster size, combined with the assumption that first-neighbor hydroxyl groups must have antiparallel orientations, results in 743 possible arrangements, containing between $n_{\mathrm{OH},j} = 0$ and $n_{\mathrm{OH},j} = 8$ hydroxyl groups per cluster, which can be organized in $J_{\mathrm{OH}} = 31$ symmetry-equivalence classes considering all possible space-group symmetry operations. The quantities characterizing the 31 clusters with respect to the cluster statistics and their electronic structure are summarized in Table I.

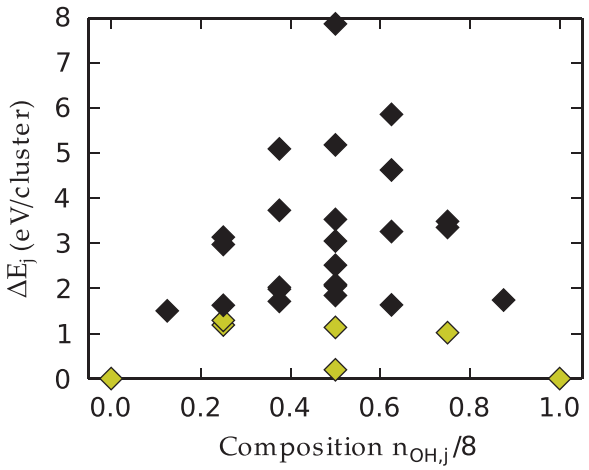

FIG. 4. Excess energies ΔE_j of cluster configurations functionalized with hydroxyl groups as a function of the number of oxygen groups per cluster $n_{\mathrm{OH},j}$. The cluster configurations with $\Delta E_j < 1.5$ eV/cluster are represented as golden diamonds, while the complementary set is represented in black.

TABLE I. Cluster classes j, their labels, their degeneracies g_j, numbers of hydroxyl groups per cluster $n_{\mathrm{OH},j}$, excess energies ΔE_j per cluster, and fundamental energy gaps from PBE ($E_{g,j}^{\mathrm{PBE}}$) and HSE06 calculations ($E_{g,j}^{\mathrm{HSE}}$).

j	Label	$n_{\mathrm{OH},j}$	g_j	ΔE_j (eV)	$E_{g,j}^{\mathrm{PBE}}$ (eV)	$E_{g,j}^{\mathrm{HSE}}$ (eV)
1	00000000	0	1	0.00	Metal	Metal
2	0000000+	1	16	1.50	1.32	1.92
3	000 + +000	2	8	1.29	2.68	3.92
4	000 + −000	2	8	1.63	2.75	3.96
5	00000 + 0+	2	24	2.97	Metal	Metal
6	00000 + 0−	2	24	3.14	Metal	Metal
7	000000 + −	2	24	1.19	0.32	0.46
8	000 + +00−	3	48	2.02	0.54	1.04
9	000 + −00+	3	48	1.98	0.88	1.53
10	000 + 0 + 0+	3	16	3.73	Metal	Metal
11	000 + 0 + 0−	3	48	5.10	Metal	Metal
12	00000 + −+	3	48	1.71	1.11	1.51
13	0 + 0 + 0 + 0+	4	4	7.87	Metal	Metal
14	0 + 0 + 0 + 0−	4	16	2.51	Metal	Metal
15	0 + 0 + 0 − 0−	4	12	5.18	Metal	Metal
16	00 + − + −00	4	12	2.09	1.61	3.21
17	00 + − − +00	4	12	1.84	2.14	3.68
18	000 + + − 0−	4	48	3.05	Metal	Metal
19	000 + − + 0+	4	48	2.06	2.02	3.11
20	000 + −0 − +	4	48	1.13	2.39	3.53
21	000 + 0 + −+	4	16	3.53	Metal	0.02
22	0000 + − + −	4	12	0.19	0.18	0.59
23	0 + 0 + 0 + −+	5	16	5.86	0.02	0.26
24	0 + 0 − 0 − +−	5	16	4.63	Metal	0.32
25	00 + − + −0−	5	48	3.26	Metal	0.05
26	000 + − + −+	5	48	1.63	0.43	1.20
27	0 + − + − + −0	6	8	3.46	Metal	0.37
28	0 + 0 + − + −+	6	24	3.35	Metal	0.79
29	00 + − + − + −	6	24	1.01	2.40	3.96
30	0 + − + − + −+	7	16	1.74	Metal	0.04
31	+ − + − + − +−	8	2	0.00	2.25	3.78

We start the investigation of the thermodynamic stability for intermediate oxidation levels by considering the excess energies ΔE_j of the 31 considered cluster classes versus the number of bonded hydroxyl groups per cluster $n_{\mathrm{OH},j}$. The considered energies were obtained from spin-polarized calculations. The calculated values are depicted in Fig. 4 and listed in Table I.

For intermediate oxidation levels the excesses energies ΔE_j are distributed in a very wide range between 0.19 eV/cluster and 7.87 eV/cluster, indeed occurring when $n_{\mathrm{OH},j} = 4$. There is a clear tendency that the most stable configurations with $\Delta E_j < 2$ eV favor the hydroxyl clustering, as can be observed for configurations $000000 + -$ ($j = 7$), $00000 + -+$ ($j = 12$), $0000 + - + -$ ($j = 22$), $000 + - + -+$ ($j = 26$), $00 + - + - + -$ ($j = 29$), and $0 + - + - + -+$ ($j = 30$) (see Table I). These are the most stable configurations for each possible number of hydroxyl groups per cluster, $2 \leqslant n_{\mathrm{OH},j} \leqslant 7$. The most energetically unfavored configuration is $0 + 0 + 0 + 0+$ ($j = 13$), which does not exhibit pairs of neighboring hydroxyls. Apart from the pure graphene ($j = 1$) and graphene oxide ($j = 31$) the most stable intermediate configuration $0000 + - + -$ ($j = 22$) represents an ordered structure with parallel zigzag chains of alternately arranged -OH groups in the direction of a hexagonal lattice vector (see site labeling in Fig. 1). This chain ordering significantly reduces the excess energy, since the repulsion of -OH groups in the vertical direction of the chains is practically not present, which is in agreement with previous investigations on graphene oxide energetics [25,26]. As a consequence of the resulting adjacent graphene-like chains the gap opening of the half-oxidized system $j = 22$ is small, only 0.6 eV. The -OH groups in understoichiometric graphene oxide with $x = 0.5$ prefer to aggregate along the armchair direction of graphene as one-dimensional chains on the basal plane, as has been demonstrated also in other theoretical studies [16,62].

The thermodynamic stability of a nonstoichiometric graphene oxide is investigated by the construction of the

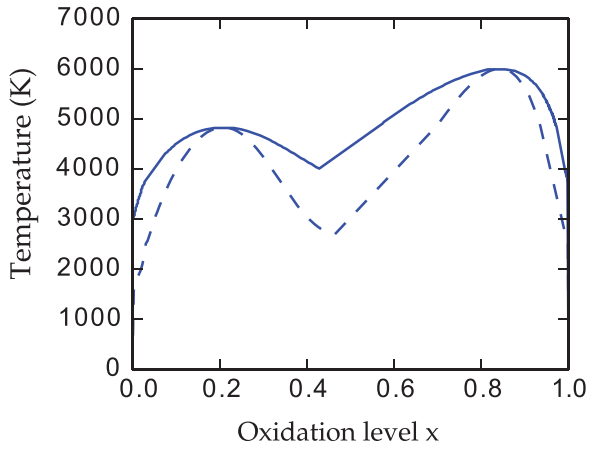

FIG. 5. The T-x phase diagram of graphene functionalized with hydroxyl groups. The binodal (spinodal) curve is represented by the full (dashed) line.

T-x phase diagram, depicted in Fig. 5, from the temperature- and composition-dependent mixing free energy $\Delta F(x,T)$. A double-peak pattern is observed in the binodal and spinodal curves, because of the low-energy chain structure $j = 22$ but also the linear chain arrangement $j = 17$ and its slightly distorted version $j = 20$. An extremely large critical temperature of $T_c = 6000$ K is calculated, meaning that graphene oxide exposed to hydroxyl groups cannot be prepared as a homogeneous phase at any oxidation level x and common growth temperatures. Both findings indicate a strong phase segregation tendency of the hydroxyl-covered graphene into oxygen-poor and -rich phases, which has been also indicated by experimental findings [22,63] and other theoretical investigations [25–27]. For higher-temperature preparation conditions and $x = 0.5$, however, one cannot exclude a partial decomposition in a third phase mainly consisting of the ordered armchair chain structure $j = 22$.

In order to estimate the average alloy properties of the nonstoichiometric graphene oxide, the alloy, according to Eq. (9), we investigate, besides room temperature, typical temperatures of 200 °C (473 K) and 1100 °C (1373 K), which represent different possible preparation conditions at which the graphene oxide samples can be produced [7].

The mean lattice constant as a function of the oxidation level x can be approximated as $a(x) = xa_{\mathrm{COH}} + (1-x)a_{\mathrm{C}} - bx(1-x)$, where b is known as the bowing parameter of the curve, because it represents the deviation of the system from Vegard's law [64,65]. Bowing parameters of $b = 0.10$ Å and $b = 0.11$ Å are calculated for the growth temperatures of $T = 473$ K and 1373 K, respectively. Therefore, mainly a linear variation with composition with only a small, almost temperature-independent bowing is found. The buckling parameter Δ (not shown) varies nonlinearly with composition from zero to the graphene oxide value. A maximum average buckling amplitude of $\Delta = 0.57$ (0.65) Å is calculated at $x = 0.64$ (0.49) for a preparation temperature of $T = 473$ K (1373 K). The observed nonmonotonic behavior of the buckling amplitude comes from cluster classes with intermediate oxidation levels that exhibit buckling amplitudes larger than 0.9 Å due to their particular arrangement of sp^2 and sp^3 carbon atoms, e.g., $j = 9, 19, 24, 26$, and 28, whose realization probabilities are enhanced for higher temperatures.

The magnetic properties of the clusters were investigated within spin-polarized simulations, considering ferromagnetic and antiferromagnetic initial configurations. In agreement with investigations made by Wang *et al.* [66], some arrangements of hydroxyl groups on the graphene sheet may exhibit ferromagnetism, electrons with unpaired spins, and nonzero magnetic moment for the ground state, e.g., $j = 13$, 14, and 23. All the configurations with excess energy $\Delta E_j < 1.5$ eV/cluster exhibit nonmagnetic ground states. In addition, we verified that class $j = 27$ exhibits an antiferromagnetic ground state. One observes that hydroxyl arrangements with such ferromagnetic and antiferromagnetic properties are restricted to large excess energies and, therefore, their realization is suppressed by thermodynamics. The average magnetic moment per cluster was calculated for the typical growth temperatures and no significant magnetization was verified.

Studying the electronic properties, we focus on the fundamental energy gap of each configuration and their average value versus oxidation level x. The definition of a fundamental gap is sometimes difficult in the case of oxidation via hydroxyl groups. The delocalized 2D π-electron distribution observed in graphene is locally or globally distorted by adsorption of hydroxyl groups. A C p_z orbital is filled with one electron which is attracted to the oxygen atom of the -OH group to form a noble gas octet shell. The interaction and π bonding of the remaining C p_z orbitals may lead to insulating or metallic cluster systems. This is illustrated in Fig. 6 for two clusters with an odd number of hydroxyls performing spin-polarized calculations. The 0000000+ ($j = 2$) cluster class exhibits in Fig. 6(a) an insulating electronic structure, with a splitting of the energy bands with different spin components large enough, so that only fully occupied or empty bands are observed. Therefore, an energy gap can be determined for such a configuration. In Fig. 6(b) the electronic band structure of the $000 + 0 + 0+$ ($j = 10$) cluster class is illustrated, exhibiting half-occupied bands and, therefore, a metallic behavior.

Fortunately, the cluster classes identified to be metallic usually have large excess energies. For that reason, we can take them into the calculation of the average fundamental gaps, since their occurrence probability is extremely small. A gap curve for intermediate compositions is obtained within the GQCA approach, weighting the fundamental gaps of the different 31 cluster configurations listed in Table I for each oxidation level. The obtained curves are depicted in Fig. 7 for three preparation temperatures.

The comparison of the gap values computed within different XC approaches in Table I shows that the hybrid functional enhances the fundamental energy gaps of semiconductor and insulator configurations compared with the PBE functional. In addition, for six highly oxidized configurations that were predicted within PBE calculations to have a metallic behavior, finite band gaps are calculated within the hybrid functional description (see Table I).

When the electronic properties are related to the excess energies, one observes a clear relationship between high excess energies and metallic behavior: all the configurations predicted to be metallic exhibit excess energies per cluster above 2.5 eV. Therefore, the realization of these high-energy

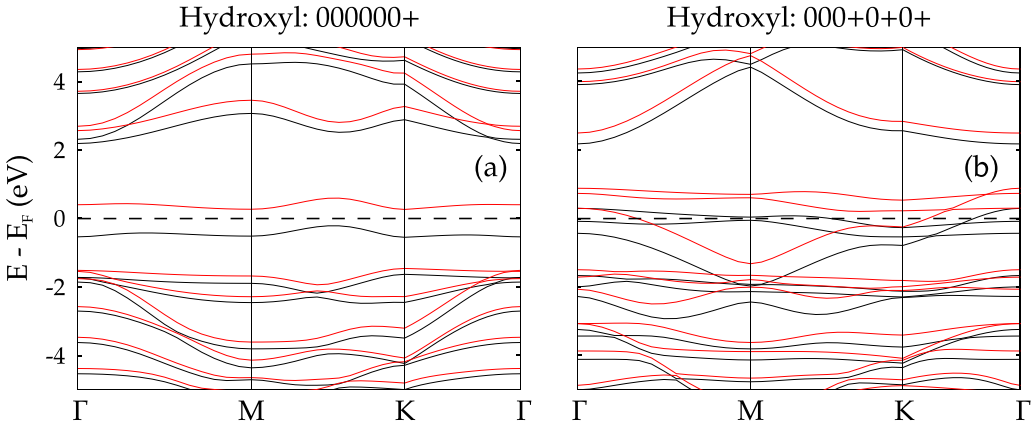

FIG. 6. Electronic band structures for cluster class configurations decorated with an odd number of hydroxyl groups per cluster obtained from spin-polarized PBE calculations. The Fermi energy level is chosen as the reference. One observes that (a) the 0000000+ ($j = 2$) cluster arrangement exhibits for each different spin channel fully (un)occupied bands, showing an insulating electronic structure; (b) the 000+0+0+ ($j = 10$) cluster class exhibits half-occupied bands, being therefore a metallic atomic arrangement.

-OH distributions is energetically less probable; i.e., these configurations are unfavorable. However, these configurations influence the average energy gap curve versus composition in Fig. 7, in particular for higher temperatures. For lower temperatures, the energy gap curve is monotonically crescent, despite the existence of metallic configurations, and only a small gap bowing is visible. For higher temperatures the energy gap curve becomes S shaped. Larger gap systems with excess energies ΔE_j near 2 eV influence the findings. Figure 7 shows that, independently of the preparation temperature, the gap can be tuned between tenths of eV until about 3.5 eV with the complete coverage by -OH groups. The big dispersion of energy gaps $E_{g,j}^{\mathrm{HSE}}$ of the considered clusters and the temperature influence of the average energy gap curves observed in Fig. 7 show the importance of taking statistics and growth conditions into account. These results are in agreement with other calculations with a screened hybrid functional [16], but also measurements of typical band gaps of 2.3–3.6 eV [67], 3.26 eV [68], 3.6 eV [69], and 2.4–4.3 eV [70] for graphene oxides.

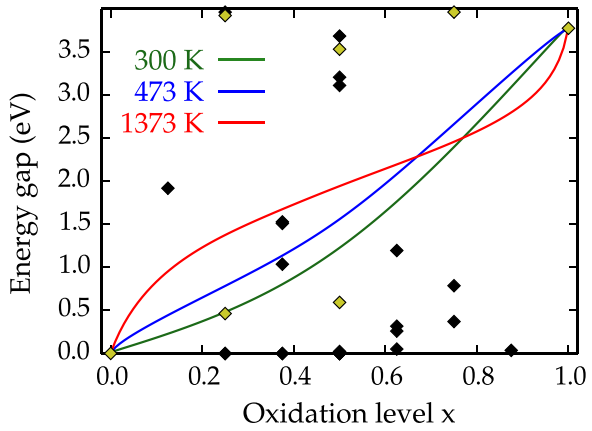

FIG. 7. Energy gap curve of graphene functionalized with hydroxyl groups as a function of the oxidation level within HSE06 framework. The diamonds represent the HSE06 energy gaps of all the cluster configurations considered, the set of cluster configurations with $\Delta E_j < 1.5$ eV/cluster are represented as golden diamonds, while the complementary set is represented with black diamonds. Metallic behavior is identified with a zero-energy gap.

The effect of synthesis temperature can be observed comparing the curves for $T = 300$ K, 473 K, and 1373 K in Fig. 7. As the temperature increases, more configurations with larger excess energies have a bigger statistical relevance and change the average energy gap curve profile. When low-oxidation levels are considered, this effect leads to enhanced occurrence probabilities of configurations with intermediate oxidation levels with larger fundamental energy gaps. For high oxidation levels, the average oxidation level constrains the statistics favoring configurations with more hydroxyl groups, and the temperature increase results in smaller energy gaps due a probability enhancement of the $0+-+-+-+$ configuration.

In Fig. 8(a) we display the absorbance spectra considering average oxidation levels $x = 0.25$, 0.50, and 0.75 considering local composition fluctuation effects, i.e., homogeneous alloys, at $T = 473$ K and 1373 K. For low temperature, one can observe that the absorbance spectra progressively change from the graphene pattern to the absorbance spectra of a fully decorated graphene sheet with -OH groups (see Fig. 3). At an oxidation level $x = 0.50$ a very wide absorbance range is expected in this case. The increase of temperature at $x = 0.25$ exhibits a secondary adsorption peak around 2.5 eV mainly associated with the 0000000+ ($j = 2$) configuration. The effect of complete phase segregation is illustrated in Fig. 8(b). In this case, the $j = 2$ cluster class still significantly contributes to the average spectrum, especially for higher temperature. However, the qualitative behavior of the optical spectra of fully phase segregated systems is dominated by the absorbance peaks associated with the graphene and fully oxidized GO phases, when the complete phase segregation is considered.

C. Partial epoxy oxidation

We consider 689 possible arrangements, containing between $n_{\mathrm{epo},j} = 0$ and $n_{\mathrm{epo},j} = 4$ epoxy groups per 2×2 cluster cell, which can be organized in $J_{\mathrm{epo}} = 24$ symmetry-

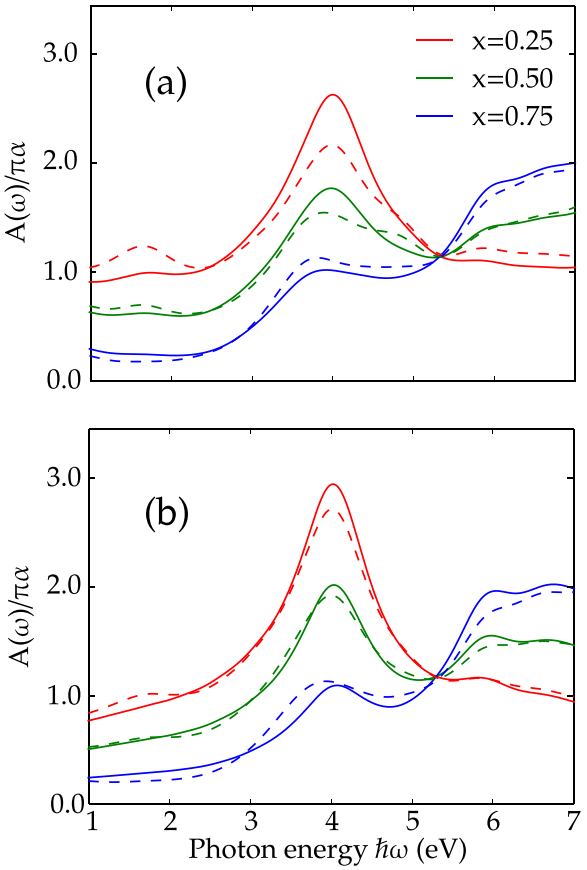

FIG. 8. Average optical absorbance as a function of the photon energy for GO systems decorated with -OH groups with oxidation levels $x = 0.25$, 0.50, and 0.75, represented as red, green, and blue curves, respectively. The average spectra are calculated at $T = 473$ K (full lines) and 1373 K (dashed lines). The adsorption spectra predictions are calculated considering only local composition fluctuations, i.e., a homogeneous alloy (a) and complete phase segregation (b).

equivalence classes with different degeneracies g_j (see Table II).

In Fig. 9 the excess energies of the 24 cluster classes listed in Table II are plotted as a function of the number of epoxy groups adsorbed per cluster. One observes that the configurations with alternated epoxy groups on top and below the graphene sheet have lower excess energies, as verified for classes $00+-00000+-0$ ($j = 20$), $00++00000--0$ ($j = 19$), and $00+00+0000--$ ($j = 23$). Cluster configurations with epoxy exposure just on one side of the carbon sheet result in larger excess energies, as occurs for the $0000000000++$ ($j = 7$), $0000++0000+0$ ($j = 9$), and $00+00+0000++$ ($j = 21$) cluster classes. On average, the excess energies ΔE_j are smaller for the -O- groups (Table II) compared to the -OH groups (Table I). Apart from zero-gap graphene the two cluster classes $j = 9$ and 10 with the largest excess energies again tend to be metallic.

The cluster configurations with $n_{\mathrm{epo},j} = 4$, apart from the configurations $j = 17$ and 21 which have epoxy groups only at on side of the graphene sheet, possess very small excess energies. Therefore, for the oxidation level $x = 1$, the fully oxidized system represents a structurally disordered system composed by clusters with a complete occupation by -O- groups (as discussed in Sec. III A). The configurations $j = 19$, 20, and 23 with $n_{\mathrm{epo},j} = 4$ and almost vanishing excess energies can be considered as ordered structures, e.g., as alternating arrangements of -O- groups along armchair

TABLE II. Cluster classes j, their labels, their degeneracies g_j, numbers of epoxy groups per cluster $n_{\mathrm{epo},j}$, excess energies ΔE_j per cluster, and fundamental energy gaps from PBE ($E_{g,j}^{\mathrm{PBE}}$) and HSE06 calculations ($E_{g,j}^{\mathrm{HSE}}$).

j	Label	$n_{\mathrm{epo},j}$	g_j	ΔE_j (eV)	$E_{g,j}^{\mathrm{PBE}}$ (eV)	$E_{g,j}^{\mathrm{HSE}}$ (eV)
1	0000000000	0	1	0.00	Metal	Metal
2	0000000000+	1	24	0.96	0.63	0.82
3	00000 + +00000	2	12	1.67	1.67	3.30
4	00000 + −00000	2	12	1.09	2.52	3.81
5	000000000 + +0	2	24	1.48	0.49	0.95
6	000000000 + −0	2	24	0.67	0.13	0.42
7	0000000000 + +	2	48	1.74	1.41	2.35
8	0000000000 + −	2	48	1.15	1.98	2.92
9	0000 + +0000 + 0	3	16	3.69	Metal	0.03
10	0000 + +0000 − 0	3	48	3.00	Metal	Metal
11	00000 + +0000+	3	24	1.95	1.96	3.64
12	00000 + +0000−	3	24	0.63	2.34	3.78
13	00000 + −0000+	3	48	0.73	3.30	4.50
14	000000 + +000+	3	48	2.17	2.53	3.84
15	000000 + +000−	3	96	0.74	2.81	4.03
16	000000 + −000+	3	48	0.98	2.95	4.17
17	00 + +00000 + +0	4	6	2.21	3.37	4.81
18	00 + +00000 + −0	4	24	0.64	3.32	5.17
19	00 + +00000 − −0	4	12	0.03	4.52	6.37
20	00 + −00000 + −0	4	6	0.00	3.12	5.05
21	00 + 00 + 0000 + +	4	12	2.81	3.96	5.58
22	00 + 00 + 0000 + −	4	48	0.77	4.31	6.24
23	00 + 00 + 0000 − −	4	24	0.01	4.09	5.50
24	00 + 00 − 0000 + −	4	12	0.29	4.36	6.33

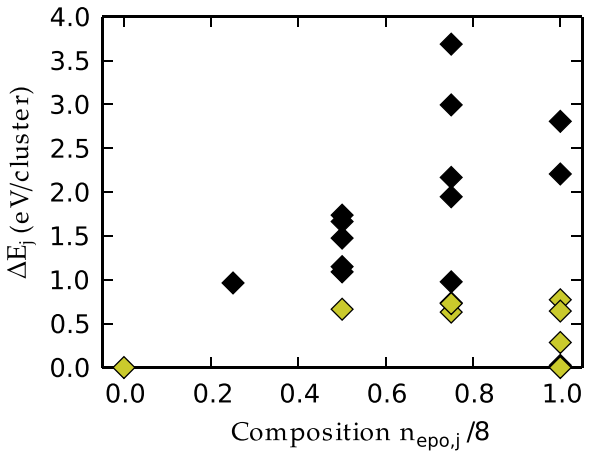

FIG. 9. Excess energies ΔE_j of cluster configurations functionalized with hydroxyl groups as a function of the number of oxygen groups per cluster $n_{\mathrm{epo},j}$. The cluster configurations with $\Delta E_j < 0.8$ eV/cluster are represented as golden diamonds, while the complementary set is represented in black.

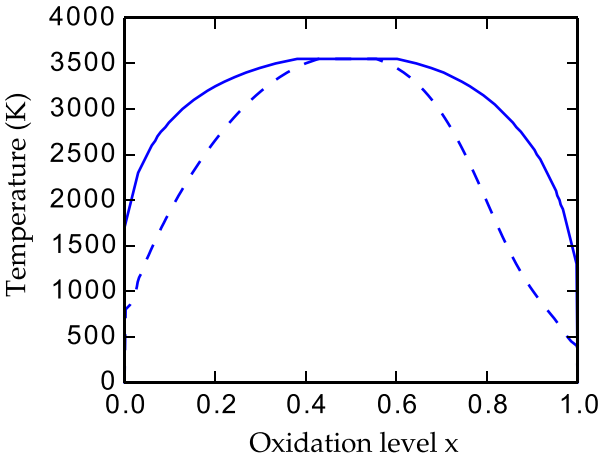

FIG. 10. The T-x phase diagram of graphene functionalized with epoxy groups. The binodal (spinodal) curve is represented by the full (dashed) line.

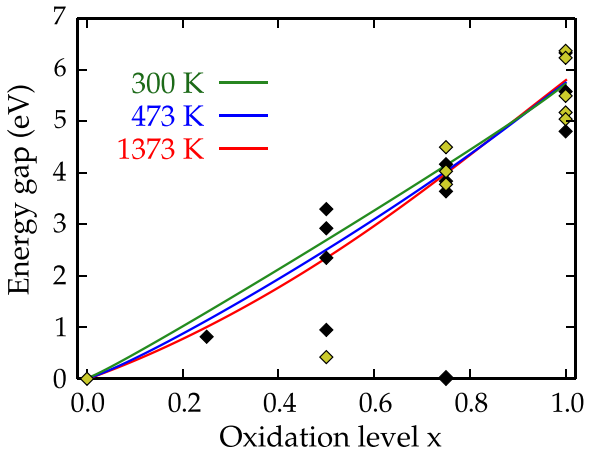

FIG. 11. Energy gap curve of graphene functionalized with epoxy groups as a function of the oxidation level within the HSE06 framework. The diamonds represent the HSE06 energy gaps of all the cluster configurations considered, the set of cluster configurations with $\Delta E_j < 0.8$ eV/cluster are represented as golden diamonds, while the complementary set is represented with black diamonds. Metallic behavior is identified with a zero-energy gap.

directions ($j = 20$). However, because of the chosen 2×2 cells no isolated chains can be extracted as in the case of 5×5 cells [16,62].

A T-x phase diagram of graphene functionalized with epoxy groups is constructed and displayed in Fig. 10. A critical temperature $T_{c,\mathrm{epo}} = 3550$ K is calculated. One can verify that temperatures above 500 K result in a pronounced increase of the possible range of oxidation level in which stable homogeneous phases can be obtained. One observes that the asymmetry of the excess energy ΔE_j distribution in Fig. 9 is not reflected in the T-x phase diagram displayed in Fig. 10. This result is explained by the fact that clusters with high oxidation levels and excess energies above 2.0 eV/cluster have significantly lower statistical weights than the ones with lower excess energies for $T < T_{c,\mathrm{epo}}$.

Comparing the two phase diagrams in Figs. 5 and 10, a tendency is visible that the epoxy groups are more likely to produce homogeneous phases with partial oxidation than hydroxyl groups. The phase diagram in Fig. 10 displays a wide range between the spinodal and binodal curves. This fact indicates that for low and high oxygen compositions the decomposition of the alloy into graphene and graphene oxide phase is hampered.

The GQCA approach predicts an almost linear behavior of the lattice constant as a function of the oxidation level x, with deviations not larger than 0.006 Å. Therefore, understoichiometric graphene oxides covered by epoxy groups follow Vegard's law [64,65]. The average buckling amplitude for intermediate oxidation levels can be well approximated as $\Delta(x) = (1-x)\Delta_{\mathrm{C}} + x\Delta_{\mathrm{epo}}(T) - bx(1-x)$, where the bowing parameters for $T = 473$ K and 1373 K are respectively -0.27 Å and -0.42 Å, i.e., exhibit an antibowing. The lengths and angles between oxygen bonds in the epoxy groups show no significant changes versus the oxidation level. Therefore, we conclude that the geometry of the epoxy groups is rather insensitive to the occupation and the orientation of the -O- groups.

Energy gap curves are plotted versus composition in Fig. 11. The average gap curve for epoxy functionalization varies between 0 eV and 5.58 eV according to the oxidation level of the samples made by understoichiometric graphene oxide. As a general tendency the addition of epoxy groups leads to an enhancement of the fundamental gap. This can be observed both in the average gap curve but also for the energy gap of the considered clusters. The energy gap curves are calculated at $T = 300$ K, 473 K, and 1373 K for comparison. One sees that the increase of the growth temperature results in a larger bowing parameter of the energy gap curve. However, the temperature dependence is less pronounced compared with the hydroxyl oxidation. A striking effect of the epoxy treatment is a further increase of the gap compared to the hydroxyl oxidation (see Fig. 7) in agreement with other *ab initio* studies [16]. The photoluminescence measurement of graphene samples subjected to O_2 plasma and annealed at 250 °C shows emission in the 350–850 nm wavelength range with a maximum emission near a photon energy of 2 eV [15]. Fluorescence studies of as-synthesized GO and such underlying a controlled deoxidation by hydrazine vapor exhibit values slightly below our prediction of about 5.6 eV for a complete decoration of graphene with epoxy groups.

Similarly to the case of graphene decoration with -OH groups, we have calculated average absorbance spectra for graphene decorated with epoxy groups for oxidation levels $x = 0.25$, 0.50, and 0.75 at $T = 473$ K and 1373 K. Figure 12(a) illustrates the optical absorption taking only composition fluctuations into account as in homogeneous alloys. Three peaks can be identified around 1.5 eV, 4.0 eV, and 7.0 eV depending on the composition and temperature. The peak at 1.5 eV is mainly associated with 00000000000+ ($j = 2$), especially for small oxidation levels and high temperatures. The peak near 4.0 eV is associated not only with the graphene cluster class ($j = 1$) but also with configurations with intermediate oxygen composition as $j = 8$, 12, 13, and 16, which give rise to a peak broadening increasing the preparation temperature for $x = 0.50$, for example. The peak in the UV region is associated with the average of

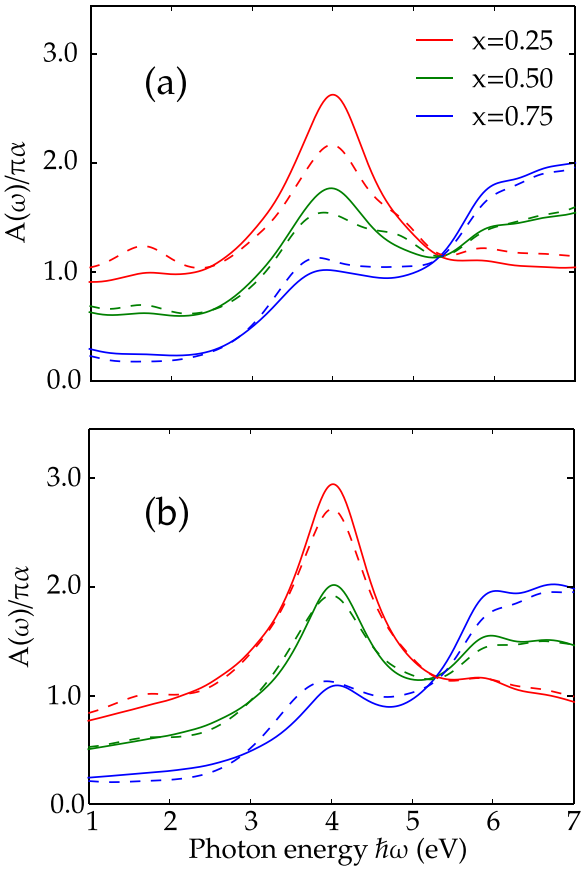

FIG. 12. Average optical absorbance as a function of the photon energy for GO systems decorated with -O- groups with oxidation levels $x = 0.25$, 0.50, and 0.75, represented as red, green, and blue curves, respectively. The average spectra are calculated at $T = 473$ K (full lines) and 1373 K (dashed lines). The adsorption spectra are calculated considering local composition fluctuations, i.e., homogeneous alloys (a) and complete phase segregation (b).

the fully oxidized cluster configurations with -O- groups. When the phase segregation effect is considered, as illustrated in Fig. 12(b), the statistical weight of configurations with intermediate oxidation levels is suppressed, and the intensity of the peak at 1.5 eV and the spectra dependence on the temperature become less pronounced.

IV. SUMMARY AND CONCLUSIONS

Applying a combination of *ab initio* total-energy and electronic structure calculations and a statistical approach to chemical and structural disorder, we have shown that chemical control of the GO samples is an interesting tool to tune energy gap and optical absorption of 2D materials.

We have adapted the generalized quasichemical approximation for the on-site adsorption, here -OH, and the occupation of bonds by other groups, here -O-. The underlying cluster expansion has been used to divide the understoichiometric 2D graphene oxides into local arrangements of functionalizing oxidant groups. The quasiparticle electronic structure of the arrangements has been studied in the framework of a hybrid functional. For the purpose of comparison also Kohn-Sham eigenvalues, also with spin polarization, have been given.

The local -COH and -C-O-C- structures depend only weakly on the oxidation level x. Interestingly, some understoichiometric oxides prefer ordered structures. Four -OH groups per 2×2 cell (i.e., $x = 0.5$) prefer to form zigzag chains along the armchair direction of the graphene basal plane. A few oxides formed with low coverages of hydroxyl groups give rise to metallic systems. Since their occurrence probabilities are, however, very small at not too high temperatures, they hardly influence the electronic and optical properties of the system. The constructed T-x phase diagrams indicate a strong tendency toward phase separation.

The results of the quasiparticle electronic structure calculations indicate that the fundamental gap of the oxides can be tuned between 0 eV and 3.6 eV (hydroxyl) or 5.6 eV (epoxy) with a clear increase of the band gap size in the case of epoxides. For not too high temperatures the dependence of the band gap on the oxidation level exhibits some bowing. For higher preparation temperatures, an S-like behavior is observed for hydroxyl adsorption. We have also investigated the optical absorbance of freestanding layers. For homogeneous alloys the spectra exhibit continuous changes of the absorption edges with the composition, while the spectra for phase-decomposed oxides show a two-mode behavior in agreement with the properties of graphene-like and graphene-oxide-like phases.

ACKNOWLEDGMENTS

We thank the Brazilian funding agencies FAPESP (Grant No. 2012/50738-3), CAPES (PVE; Grants No. 88881.068355/2014-01 and No. 88887.116535/2016-00), and CNPQ (Grants No. 305405/2014-4 and No. 308742/2016-8) for the financial support. The authors acknowledge the National Laboratory for Scientific Computing (LNCC/MCTI, Brazil) for providing HPC resources of the SDumont supercomputer.

APPENDIX: PROOF OF EQUIVALENCE BETWEEN SHANNON ENTROPY AND RESULTS FROM COMBINATORICS

1. Entropy of random alloys

Starting from the simplest case, which is a binary substitutional alloy with N atomic sites that can be occupied by $N_A = xN$ atoms A and $N_B = (1-x)N$ atoms B. The alloy can be divided into M local atomic arrangements, called clusters, with $n = N/M$ sites. According to the system structure, the possible arrangements can be organized in symmetry-equivalent classes $j = 1, 2, \ldots, J$ with respective degeneracies g_j. From basic combinatorics, one well knows that the number of possible atomic arrangements in the system is given by

$$\Omega_0 = \frac{N!}{N_A! N_B!}. \tag{A1}$$

The corresponding configurational entropy can be calculated from the Boltzmann definition $S_0 = k_b \ln \Omega_0$. Within the

Stirling approximation, the entropy results as

$$S_0 = -Nk_b[x \ln x + (1-x)\ln(1-x)]. \quad \text{(A2)}$$

In a binary random alloy, the set of probabilities for realization of a cluster class j is determined by the average composition x of element A, y of element B ($x + y = 1$), and the degeneracy of each cluster class as

$$x_j^o = g_j x^{n_{A,j}} y^{n_{B,j}}, \quad \text{(A3)}$$

with $n_{A,j}$ ($n_{B,j}$) representing the number of A (B) atoms in cluster j.

Substituting this random probability distribution in the entropy expression (5), one obtains a configurational entropy

$$S_0 = -k_b M \left(\sum_{j=1}^{J} x_j n_{A,j} \ln x + \sum_{j=1}^{J} x_j n_{B,j} \ln y \right). \quad \text{(A4)}$$

The average composition constraints $\sum_{j=1}^{J} x_j n_{A,j} = nx$ and $\sum_{j=1}^{J} x_j n_{B,j} = ny$ yield the same result as (A2). This equivalence of the two approaches can be easily generalized for random alloys of more atomic components.

2. Entropy of cluster expansion within GQCA

The configurational entropy of the system per cluster obtained within the GQCA is given by the expression (see [30,32,36,37,71])

$$\Delta S = -Nk_b(x \ln x + y \ln y) - k_b M \sum_{j=1} x_j \ln\left(\frac{x_j}{x_j^o}\right), \quad \text{(A5)}$$

which consists of the entropy S_0 (A2) obtained from combinatoric arguments, but is modified by deviations of probabilities x_j of the possible atomic arrangements from *a priori* probabilities x_j^o [37]. It is also known that the ways of performing corrections on the number Ω compared to Ω_0 (A1) that result in the same expression in the Stirling limit are not unique [71].

The correction term on entropy has a clear correspondence in information theory. The Kullback-Leibler divergence [40] associated with the increase of entropy is associated with the assumption of a probability distribution among the several clusters x_j^o instead of x_j, considered to be the correct probability distribution.

The equivalence between the configurational and informational entropy expressions has been demonstrated for the ideal solid solution case and is also valid for the entropy estimated within GQCA. The difference δS between the entropy values per cluster calculated from (A5) and (5) is

$$\delta S = -k_b \sum_{j=1}^{J} x_j \left(\frac{g_j}{x_j}\right) + k_b \sum_{j=1}^{J} x_j^o \left(\frac{g_j}{x_j^o}\right) + k_b \sum_{j=1}^{J} x_j ln\left(\frac{x_j}{x_j^o}\right) \quad \text{(A6)}$$

and

$$\delta S = -k_b \sum_{j=1}^{J} (x_j - x_j^o) \ln\left(\frac{g_j}{x_j^o}\right). \quad \text{(A7)}$$

Substituting the random probability distribution x_j^o, given by (A3) in the logarithm, we obtain that

$$\delta S = k_b \left\{ \left[\sum_{j=1}^{J} x_j^o n_{A,j} - \sum_{j=1}^{J} x_j n_{A,j} \right] \ln x + \left[\sum_{j=1}^{J} x_j^o n_{B,j} - \sum_{j=1}^{J} x_j n_{B,j} \right] \ln y \right\}. \quad \text{(A8)}$$

Since the *a priori* and *a posteriori* probability distributions x_j^o and x_j refer to the same system, the terms in square brackets cancel each other because the average composition x is a given constraint. Therefore,

$$\delta S = 0 \quad \text{(A9)}$$

holds, and the informational and configurational approaches lead to the same result.

[1] A. K. Geim and K. S. Novoselov, Nat. Mater. **6**, 183 (2007).
[2] S. Park and R. S. Ruoff, Nat. Nanotechnol. **4**, 217 (2009).
[3] S. Eigler and A. Hirsch, Angew. Chem., Int. Ed. **53**, 7720 (2014).
[4] K. P. Loh, Q. Bao, G. Eda, and M. Chhowalla, Nat. Chem. **2**, 1015 (2010).
[5] S. Mao, H. Pu, and J. Chen, RSC Adv. **2**, 2643 (2012).
[6] D. R. Dreyer, S. Park, C. W. Bielawski, and R. S. Ruoff, Chem. Soc. Rev. **39**, 228 (2010).
[7] S. Pei and H.-M. Cheng, Carbon **50**, 3210 (2012).
[8] C. Gómez-Navarro, R. T. Weitz, A. M. Bittner, M. Scolari, A. Mews, M. Burghard, and K. Kern, Nano Lett. **7**, 3499 (2007).
[9] Z. Wei, D. Wang, S. Kim, S.-Y. Kim, Y. Hu, M. K. Yakes, A. R. Laracuente, Z. Dai, S. R. Marder, C. Berger, W. P. King, W. A. de Heer, P. E. Sheehan, and E. Riedo, Science **328**, 1373 (2010).
[10] X. Wu, M. Sprinkle, X. Li, F. Ming, C. Berger, and W. A. de Heer, Phys. Rev. Lett. **101**, 026801 (2008).
[11] G. Eda, G. Fanchini, and M. Chhowalla, Nat. Nanotechnol. **3**, 270 (2008).
[12] J. T. Robinson, F. K. Perkins, E. S. Snow, Z. Wei, and P. E. Sheehan, Nano Lett. **8**, 3137 (2008).
[13] V. Dua, S. Surwade, S. Ammu, S. Agnihotra, S. Jain, K. Roberts, S. Park, R. Ruoff, and S. Manohar, Angew. Chem. **122**, 2200 (2010).
[14] J. Zhang and X. S. Zhao, J. Phys. Chem. C **116**, 5420 (2012).
[15] A. Nourbakhsh, M. Cantoro, T. Vosch, G. Pourtois, F. Clemente, M. H. van der Veen, J. Hofkens, M. M. Heyns, S. D. Gendt, and B. F. Sels, Nanotechnology **21**, 435203 (2010).
[16] X. Jiang, J. Nisar, B. Pathak, J. Zhao, and R. Ahuja, J. Catal. **299**, 204 (2013).
[17] B. C. Brodie, Philos. Trans. R. Soc. London **149**, 249 (1859).
[18] W. S. Hummers Jr. and R. E. Offeman, J. Am. Chem. Soc. **80**, 1339 (1958).

[19] W. Cai, R. D. Piner, F. J. Stadermann, S. Park, M. A. Shaibat, Y. Ishii, D. Yang, A. Velamakanni, S. J. An, M. Stoller, J. An, D. Chen, and R. S. Ruoff, Science **321**, 1815 (2008).
[20] H. He, T. Riedl, A. Lerf, and J. Klinowski, J. Phys. Chem. **100**, 19954 (1996).
[21] U. Hofmann and R. Holst, Ber. Dtsch. Chem. Ges. (A and B Series) **72**, 754 (1939).
[22] H. He, J. Klinowski, M. Forster, and A. Lerf, Chem. Phys. Lett. **287**, 53 (1998).
[23] G. Ruess, Monatshefte für Chemie und verwandte Teile anderer Wissenschaften **76**, 381 (1947).
[24] C. Soldano, A. Mahmood, and E. Dujardin, Carbon **48**, 2127 (2010).
[25] J.-A. Yan, L. Xian, and M. Y. Chou, Phys. Rev. Lett. **103**, 086802 (2009).
[26] J.-A. Yan and M. Y. Chou, Phys. Rev. B **82**, 125403 (2010).
[27] H. Zhou, M. Zhao, X. Zhang, W. Dong, X. Wang, H. Bu, and A. Wang, J. Phys.: Condens. Matter **25**, 395501 (2013).
[28] M. C. Kim, G. S. Hwang, and R. S. Ruoff, J. Chem. Phys. **131**, 064704 (2009).
[29] N. Lu, D. Yin, Z. Li, and J. Yang, J. Phys. Chem. C **115**, 11991 (2011).
[30] L. K. Teles, J. Furthmüller, L. M. R. Scolfaro, J. R. Leite, and F. Bechstedt, Phys. Rev. B **62**, 2475 (2000).
[31] L. K. Teles, L. G. Ferreira, L. M. R. Scolfaro, and J. R. Leite, Phys. Rev. B **69**, 245317 (2004).
[32] I. Guilhon, L. K. Teles, M. Marques, R. R. Pela, and F. Bechstedt, Phys. Rev. B **92**, 075435 (2015).
[33] F. L. Freitas, J. Furthmüller, F. Bechstedt, M. Marques, and L. K. Teles, Appl. Phys. Lett. **108**, 092101 (2016).
[34] I. Guilhon, M. Marques, L. K. Teles, and F. Bechstedt, Phys. Rev. B **95**, 035407 (2017).
[35] R. R. Pela, M. Marques, and L. K. Teles, J. Phys.: Condens. Matter **27**, 505502 (2015).
[36] A. Sher, M. van Schilfgaarde, A.-B. Chen, and W. Chen, Phys. Rev. B **36**, 4279 (1987).
[37] M. Marques, L. K. Teles, L. G. Ferreira, L. M. R. Scolfaro, J. Furthmüller, and F. Bechstedt, Phys. Rev. B **73**, 235205 (2006).
[38] F. Romá, A. J. Ramirez-Pastor, and J. L. Riccardo, Langmuir **19**, 6770 (2003).
[39] M. Dávila, F. Romá, J. Riccardo, and A. Ramirez-Pastor, Surf. Sci. **600**, 2011 (2006).
[40] S. Kullback and R. A. Leibler, Ann. Math. Statist. **22**, 79 (1951).
[41] C. E. Shannon, Bell Syst. Tech. J. **27**, 379 (1948).
[42] G. Kresse and J. Furthmüller, Comput. Mater. Sci. **6**, 15 (1996).
[43] G. Kresse and J. Hafner, Phys. Rev. B **47**, 558(R) (1993).
[44] J. P. Perdew, K. Burke, and M. Ernzerhof, Phys. Rev. Lett. **77**, 3865 (1996).
[45] J. P. Perdew, K. Burke, and M. Ernzerhof, Phys. Rev. Lett. **78**, 1396 (1997).
[46] P. E. Blöchl, Phys. Rev. B **50**, 17953 (1994).
[47] G. Kresse and D. Joubert, Phys. Rev. B **59**, 1758 (1999).
[48] H. J. Monkhorst and J. D. Pack, Phys. Rev. B **13**, 5188 (1976).
[49] L. G. Ferreira, M. Marques, and L. K. Teles, Phys. Rev. B **78**, 125116 (2008).
[50] F. Bechstedt, *Many-Body Approach to Electronic Excitations* (Springer-Verlag, Berlin, 2015).
[51] J. Heyd, G. E. Scuseria, and M. Ernzerhof, J. Chem. Phys. **118**, 8207 (2003).
[52] J. Heyd, G. E. Scuseria, and M. Ernzerhof, J. Chem. Phys. **124**, 219906 (2006).
[53] B. Adolph, V. I. Gavrilenko, K. Tenelsen, F. Bechstedt, and R. Del Sole, Phys. Rev. B **53**, 9797 (1996).
[54] M. Gajdoš, K. Hummer, G. Kresse, J. Furthmüller, and F. Bechstedt, Phys. Rev. B **73**, 045112 (2006).
[55] L. Yang, J. Deslippe, C.-H. Park, M. L. Cohen, and S. G. Louie, Phys. Rev. Lett. **103**, 186802 (2009).
[56] L. Wirtz, A. Marini, and A. Rubio, Phys. Rev. Lett. **96**, 126104 (2006).
[57] L. Matthes, O. Pulci, and F. Bechstedt, New J. Phys. **16**, 105007 (2014).
[58] W. Mönch, *Semiconductor Surfaces and Interfaces* (Springer, Berlin, 1993).
[59] O. Pulci, P. Gori, M. Marsili, V. Garbuio, R. Del Sole, and F. Bechstedt, Europhys. Lett. **98**, 37004 (2012).
[60] L. Matthes, P. Gori, O. Pulci, and F. Bechstedt, Phys. Rev. B **87**, 035438 (2013).
[61] R. R. Nair, P. Blake, A. N. Grigorenko, K. S. Novoselov, T. J. Booth, T. Stauber, N. M. R. Peres, and A. K. Geim, Science **320**, 1308 (2008).
[62] L. Wang, Y. Y. Sun, K. Lee, D. West, Z. F. Chen, J. J. Zhao, and S. B. Zhang, Phys. Rev. B **82**, 161406 (2010).
[63] A. Lerf, H. He, M. Forster, and J. Klinowski, J. Phys. Chem. B **102**, 4477 (1998).
[64] L. Vegard, Z. Phys. **5**, 17 (1921).
[65] A. R. Denton and N. W. Ashcroft, Phys. Rev. A **43**, 3161 (1991).
[66] M. Wang, W. Huang, M. B. Chan-Park, and C. M. Li, Nanotechnology **22**, 105702 (2011).
[67] T.-F. Yeh, F.-F. Chan, C.-T. Hsieh, and H. Teng, J. Phys. Chem. C **115**, 22587 (2011).
[68] K. Krishnamoorthy, M. Veerapandian, R. Mohan, and S.-J. Kim, Appl. Phys. A **106**, 501 (2012).
[69] X. Peng, F. Tang, and A. Copple, J. Phys.: Condens. Matter **24**, 075501 (2012).
[70] T.-F. Yeh, J.-M. Syu, C. Cheng, T.-H. Chang, and H. Teng, Adv. Funct. Mater. **20**, 2255 (2010).
[71] A. B. Chen and A. Sher, *Semiconductor Alloys* (Plenum, New York, 1995).